Journal of
Materials Chemistry A

ROYAL SOCIETY
OF CHEMISTRY

PAPER

View Article Online
View Journal | View Issue

Check for updates

Cite this: *J. Mater. Chem. A*, 2024, **12**, 23035

Band engineering in iron and silver co-doped double perovskite nanocrystals for selective photocatalytic CO_2 reduction†

Razi Ahmad,*[a] Yu Zhang,[a] Jan Navrátil,[ab] Piotr Błoński,[ae] Lukáš Zdražil,[af] Sergii Kalytchuk,[a] Alberto Naldoni,*[ac] Andrey L. Rogach,[de] Michal Otyepka,[ae] Radek Zboril*[af] and Štěpán Kment*[af]

Received 29th January 2024
Accepted 18th July 2024

DOI: 10.1039/d4ta00676c

rsc.li/materials-a

Double metal cation halide perovskites are promising alternatives to lead halide perovskites due to their exceptional compositional flexibility and stability. However, their utilization in solar-light harvesting applications has been hindered by their large band gap and the complexity of producing doped or alloyed materials with desirable optoelectronic properties. In this study, we report the colloidal synthesis of iron-doped $Cs_2NaInCl_6$ double perovskite nanocrystals (NCs), leading to a significant extension of the absorption edge from 330 nm to 505 nm. We also demonstrate that simultaneous doping with Fe^{3+} and Ag^+ ions allows significant reduction of the optical band gap and precise tuning of electronic band structures of the resulting NCs. The enhanced absorption in the visible region is attributed to the substitution of In-5s by the Fe-3d state, while the introduction of the Ag 4d state upshifts the valence band maximum, inducing a transformative change in the band structure, as confirmed by density functional theory (DFT) calculations. Remarkably, by precisely controlling the band positions of the Fe^{3+}-doped $Cs_2Ag_{0.5}Na_{0.5}InCl_6$ NCs, we accomplished the selective photocatalytic reduction of CO_2 into CH_4, making them readily available for solar-energy conversion technologies.

Introduction

Solution-processable hybrid lead halide perovskites have garnered unprecedented attention in the realm of low-cost optoelectronic devices, thanks to their remarkable optical and electronic properties.[1] These materials exhibit a large absorption coefficient, high charge carrier mobility, long diffusion length, and useful defect tolerance, leading to significant advancements in optoelectronic devices like solar cells and light-emitting diodes.[2,3] However, the practical utilization of lead-based perovskite materials faces two major obstacles: poor long-term stability and toxicity concerns.[4] Consequently, significant efforts have been dedicated to the exploration of stable and environmentally benign materials, aiming to achieve optical and electronic properties comparable to those of lead halide perovskites.[5–10] Among these, lead-free halide double perovskites (DPs) with a formula $A_2M^IM^{III}X_6$ (where $A = Cs^+$, and $X = Cl^-, Br^-, I$) can be formed by heterovalent substitution of Pb^{2+} cations with a pair of monovalent ($M^I = Na^+, K^+, Ag^+$) and trivalent ($M^{III} = Bi^{3+}, Sb^{3+}, In^{3+}$) cations. They have attracted considerable attention due to several desirable features, including superior material stability, less toxic elements, compositional flexibility, and attractive optoelectronic properties.[9–11] Specifically, Cs_2AgBiX_6 ($X = Br, Cl$), $Cs_2AgInCl_6$, and $Cs_2NaInCl_6$ have been recognized as promising candidates across a diverse spectrum of applications. These encompass solar cells, photocatalysis, light-emitting diodes, luminescent solar concentrators, and scintillators.[12–16] In particular, $Cs_2AgBiBr_6$ is the only example of DP that has been extensively investigated as a lead-free light absorber layer in perovskite solar cells and as a photocatalyst for CO_2 reduction, H_2 production and organic synthesis.[13,17–22] However, $Cs_2AgBiBr_6$ DP has an indirect band gap, which is not ideal for optoelectronic and photocatalytic applications as both photons and phonons are involved in the optical absorption and recombination processes, which results in relatively weak oscillator

---

[a] *Regional Centre of Advanced Technologies and Materials, Czech Advanced Technology and Research Institute, Palacký University Olomouc, Šlechtitelů 27, Olomouc, 783 71, Czech Republic. E-mail: razi.ahmad@upol.cz; radek.zboril@upol.cz; stepan.kment@upol.cz*

[b] *Department of Physical Chemistry, Faculty of Science, Palacký University Olomouc, 17. listopadu 1192/12, 779 00 Olomouc, Czech Republic*

[c] *Department of Chemistry, NIS Centre, University of Turin, Turin 10125, Italy. E-mail: alberto.naldoni@unito.it*

[d] *Department of Materials Science and Engineering, Center for Functional Photonics (CFP), City University of Hong Kong, 83 Tat Chee Avenue, Hong Kong SAR, China*

[e] *IT4Innovations, VŠB – Technical University of Ostrava, 17. listopadu 2172/15, 708 00 Ostrava-Poruba, Czech Republic*

[f] *Nanotechnology Centre, Centre for Energy and Environmental Technologies, VŠB–Technical University of Ostrava, 17. listopadu 2172/15, 708 00 Ostrava-Poruba, Czech Republic*

† Electronic supplementary information (ESI) available. See DOI: https://doi.org/10.1039/d4ta00676c

strength for optical absorption and low photoluminescence (PL) quantum yields (QY), respectively. Thus, despite the commendable material stability and direct band gap characteristics exhibited by $Cs_2AgInCl_6$ and $Cs_2NaInCl_6$, these DP materials are not suitable for solar cells and photocatalysis application due to a large (∼4 eV) and parity-forbidden band gap.

Previous studies have demonstrated that doping and/or alloying are promising strategies to significantly alter the optical and electronic properties of DPs.[14,23,24] For example, Sb^{3+}, Sn^{2+}, Cu^+ and Fe^{3+} doping of $Cs_2AgBiBr_6$ DP materials has been used to enhance their light absorption capability, resulting in a broadband absorption range from the visible to the NIR region.[25–28] Similarly, Fe^{3+} has been incorporated into $Cs_2AgInCl_6$ DPs, demonstrating extended absorption near ≈800 nm.[29,30] Nevertheless, the majority of doping strategies aimed at enhancing light absorption have been predominantly focused on single crystals or microcrystals of DPs. Consequently, the optoelectronic and photocatalytic applications of doped/alloyed DPs have been hindered due to their limited solubility in common organic solvents, which is highly desirable for thin-film processing *via* the spin/dip coating method and to obtain stable colloidal dispersions for photocatalysis. In this regard, the colloidal synthesis of doped/alloyed DP nanocrystals (NCs) is an attractive strategy to overcome these limitations and make them available for solar-energy conversion technologies.[13,19,31]

In the case of DP NCs, however, there remains a necessity to implement doping strategies for the purpose of fine-tuning their electronic and optical properties. For instance, diverse transition metals and lanthanide ions have been introduced into Cs_2MInCl_6 (M = Ag, Na) chloride-based DP NCs to improve their PLQYs, with the aim of utilizing them in light emitting diodes.[31–38] Another challenging aspect of compositional engineering for DP NCs involves the precise control over the doping concentration. Ning *et al.* used a Bi : Fe molar ratio of 3 : 2 to achieve only 1.4% Fe doping in $Cs_2AgBiBr_6$ single crystals.[39] In another report by Liu *et al.*, approximately 1% of Fe ions w.r.t. Bi ions were successfully incorporated into the $Cs_2AgBiBr_6$ lattice, when equimolar ratio of Fe and Bi precursors were used during synthesis.[27] Han *et al.* emphasized the formidable challenge associated with synthesizing Fe-based DP NCs using a colloidal route, an attempt that ultimately yielded unsuccessful results.[40] The formation of the desired composition and phase of DP NCs requires precise control on growth kinetics. In other words, the fast reaction kinetics along with balanced reactivity of precursors during nucleation and growth is critical to achieve the desired composition of DP NCs.[36,41] In this context, the utilization of a highly reactive halide source could be advantageous to initiate the prompt nucleation and growth processes that may result in the desired chemical composition and optoelectronic properties.

Herein, we introduce the colloidal synthesis of Fe^{3+}-doped $Cs_2Ag_xNa_{1-x}InCl_6$ ($x = 0$, 0.5 and 1) DP NCs, and demonstrate their application in photocatalytic CO_2 reduction. Iron doping significantly extends the absorption edge of $CsNaInCl_6$ NCs from 330 nm to 505 nm. Moreover, simultaneous doping by Fe^{3+} and Ag^+ allows for significant reduction in the optical band gap and electronic band structure tuning of $CsNaInCl_6$ NCs. Electron paramagnetic resonance (EPR) measurements reveal that iron is incorporated in the Fe^{3+} state, which apparently replaces In^{3+} sites in the host DP NCs. Importantly, the Fe^{3+}-doped DP NCs tolerated polar solvents during the purification process, which is highly desirable for their application in thin-film devices and photocatalysis. The purified NCs exhibited high colloidal and structural stability under ambient conditions due to efficient surface passivation with dual cationic ligands. The Fe- and Ag- co-doped $Cs_2NaInCl_6$ DP NCs are explored for photocatalytic CO_2 reduction and demonstrate selective reduction of CO_2 into CH_4 due to favourable energetic band edge positions. We employed density functional theory (DFT) calculations to substantiate that by co-doping $Cs_2NaInCl_6$ DPs with iron and silver, we can significantly enhance their light absorption, enhance charge separation efficiency, and adjust the reduction potentials. Furthermore, this compositional modification boosts CO_2 adsorption and activation, so these synergistic improvements are crucial for the selective reduction of CO_2 to methane (CH_4). Our findings introduce a new approach for the design and synthesis of highly stable lead-free DP NCs that can be processed and employed in a variety of optoelectronic applications, including photocatalysis.

Experimental section

Materials

Cesium carbonate (99.99%), silver nitrate (99.9%), indium(III) acetate (99.99%), iron(III) acetylacetonate (99.99%), 1-octadecene (ODE, 90%), oleic acid (OA, 90%), oleylamine (OLA, 90%), trioctylphosphine (TOP, 90%), benzoyl chloride (98%), and methyl acetate (99.5%) were purchased from Sigma Aldrich; sodium acetate (99%) was purchased from Alfa Aesar. All chemicals were used without any further purification.

Synthesis of $Cs_2Ag_xNa_{1-x}InCl_6$ ($x = 0$, 0.5 and 1) NCs

In a typical synthesis of $Cs_2NaInCl_6$ NCs, cesium carbonate (0.3 mmol), sodium acetate (0.3 mmol), indium(III) acetate (0.3 mmol), ODE (10 mL), OA (1 mL), and OLA (0.5 mL) were loaded in a four-neck flask under a N_2 atmosphere. The reaction mixture was heated to 110 °C under continuous stirring for 20 min. At this stage all precursors were fully dissolved and the solution became optically clear, then 0.3 mL TOP was injected into the hot reaction mixture and the solution was kept for another 10 min under N_2 protection. Next, the temperature of the solution was increased to 140 °C and 300 μL benzoyl chloride was swiftly injected into the hot reaction mixture which initiated a prompt nucleation and growth process, indicating the formation of $Cs_2NaInCl_6$ NCs. After 5 s, the reaction mixture was rapidly cooled down in an ice-water bath.

$Cs_2Ag_{0.5}Na_{0.5}InCl_6$ alloyed NCs were synthesized by a similar procedure as mentioned above, with slight modifications. In brief, 0.3 mmol of cesium carbonate, 0.3 mmol indium(III) acetate, 0.15 mmol sodium acetate, and 10 mL of ODE together with 1 mL OA and 0.5 mL OLA were heated to 110 °C under vigorous stirring in a N_2 atmosphere. Once the reaction solution became clear and transparent, 0.3 mL TOP followed by pre-mixed Ag–TOP solution (0.15 mmol $AgNO_3$ in 0.15 mL TOP) was sequentially injected into the hot reaction mixture and the solution was kept for another 10 min under N_2 protection. For the synthesis of $Cs_2AgInCl_6$ NCs, sodium acetate was completely replaced by Ag–TOP solution (0.3 mmol $AgNO_3$ in 0.3 mL TOP). Finally, the reaction flask was heated to 140 °C and 300 μL of neat benzoyl chloride was swiftly injected into the hot reaction mixture which resulted in prompt nucleation and growth of NCs. After 5 s, the reaction flask was rapidly cooled down in an ice-water bath.

Synthesis of Fe^{3+}-doped $Cs_2Ag_xNa_{1-x}InCl_6$ ($x = 0$, 0.5 and 1) NCs

Fe^{3+}-doped $Cs_2Ag_xNa_{1-x}InCl_6$ ($x = 0$, 0.5 and 1) NCs were synthesized by the same procedure mentioned above by the substitution of indium(III) acetate with iron(III) acetylacetonate, while amounts of the other precursors and synthesis conditions remained the same. In the precursor solution, 25% and 50% iron(III) acetylacetonate substitute an equimolar amount of indium(III) acetate, while the total amount of iron(III) acetylacetonate and indium(III) acetate was fixed to 0.3 mmol. Upon benzoyl chloride injection, the color of reaction mixture was rapidly changed from dark red to yellow or yellow-orange or orange-red color depending upon the Na/Ag composition, indicating the formation of Fe^{3+}-doped $Cs_2Ag_xNa_{1-x}InCl_6$ ($x =$ 0, 0.5 and 1) NCs.

Photocatalytic CO_2 reduction experiments

The CO_2 reduction experiments were performed in a sealed Pyrex bottle loaded with an ethyl acetate/isopropanol mixture. In a typical reaction, 3 mg of extensively washed and dried NC powder were dispersed in a solvent mixture of 24 mL ethyl acetate and 1 mL of isopropanol. The reactor was purged with CO_2 for about 30 min in order to eliminate air and to form a saturated CO_2 atmosphere. The photocatalytic reaction was initiated by illuminating the reactor with a light source of intensity 150 mW cm^{-2} using a solar simulator equipped with an AM 1.5G filter. The photocatalytic reaction was performed for 6 h at room temperature. The photocatalytic reaction products were quantified through headspace gas analysis by gas chromatography with a flame ionization detector.

Results and discussion

Synthesis and purification of iron and silver co-doped double perovskite nanocrystals

Fe^{3+}-doped $Cs_2Ag_xNa_{1-x}InCl_6$ ($x = 0$, 0.5 and 1) DP NCs were synthesized based on a previously developed colloidal hot injection approach with slight modifications (see the schematic illustration of the synthesis procedure in Scheme 1).[35,36] This approach relies on the use of strongly coordinated silver–

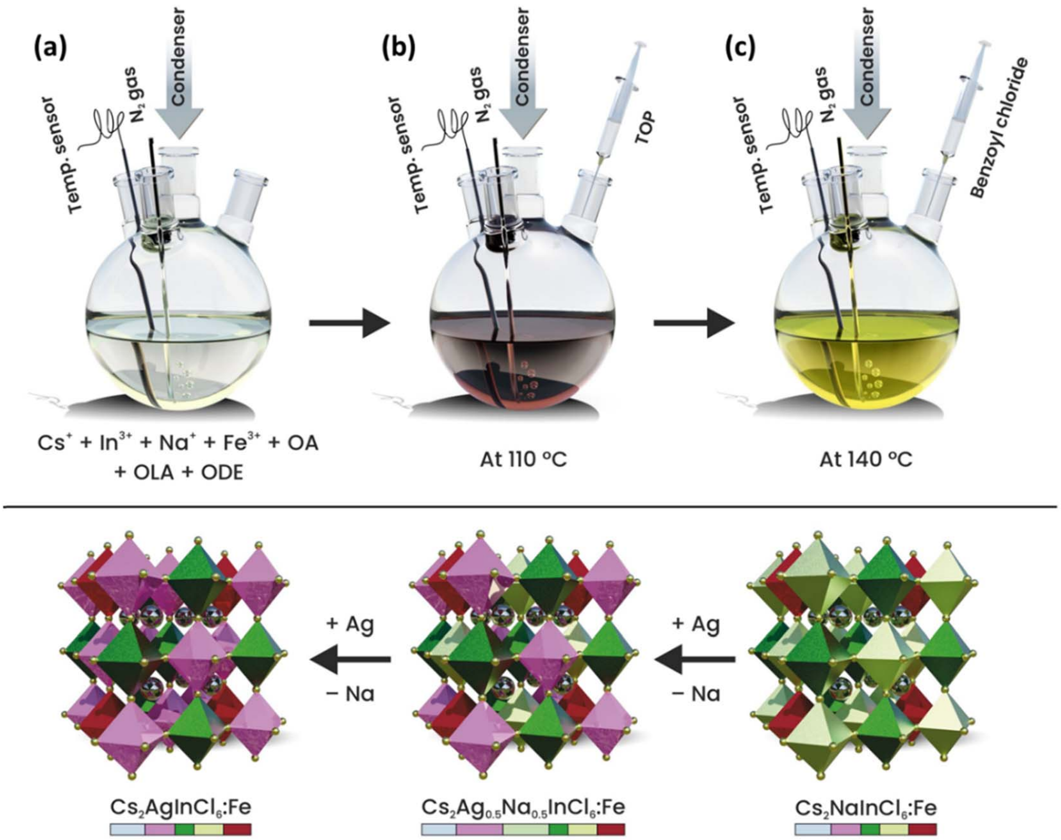

Scheme 1 Schematic illustration of the colloidal synthesis of Fe^{3+}-doped $Cs_2Ag_xNa_{1-x}InCl_6$ ($x = 0$, 0.5 and 1) DP nanocrystals.

trioctylphosphine (Ag–TOP) and benzoyl chloride as the alternative silver and chloride source, respectively, along with an additional TOP ligand. The Ag–TOP precursor is a better choice to prevent the reduction of silver ions by oleylamine (OLA) into metallic silver.[35] On the other hand, benzoyl chloride is well known for strong reactivity toward nucleophilic compounds (amines and carboxylic acids) in which the reactive CO–Cl bonds can interact with amines and/or carboxylic acids and release HCl. Moreover, TOP can facilitate the nucleophilic reaction with benzoyl chloride or HCl that results in the formation of phosphonium chloride intermediates which can serve as both halide sources and surface capping ligands.[36] In a typical synthesis of Fe^{3+}-doped $Cs_2NaInCl_6$ DP NCs, cesium carbonate, sodium acetate, indium(III) acetate, and iron(III) acetylacetonate along with oleic acid (OA), OLA and 1-octadecene (ODE) were mixed and heated at 110 °C under N_2 protection for 20 min so that the precursors were completely dissolved (Scheme 1a). After that, 300 μL of TOP was injected into the hot reaction solution, and the solution was kept for another 10 min. Subsequently, the temperature of the reaction mixture was increased to 140 °C (Scheme 1b). Finally, 300 μL of neat benzoyl chloride was injected into the hot reaction solution and the color of precursor solution was rapidly changed from dark red to yellow indicating the prompt nucleation and growth of the DP NCs (Scheme 1c). After 5 s, the mixture was rapidly immersed in an ice-cooled water bath to quench the reaction. The Fe^{3+}-doped $Cs_2Ag_{0.5}Na_{0.5}InCl_6$ and $Cs_2AgInCl_6$DP NCs were synthesized following the same approach, by simply replacing the sodium precursor with a silver precursor. The detailed description of the synthetic procedures and the purification method are provided in the Experimental section and Fig. S1 (ESI†). The following samples were prepared: Fe^{3+}-doped $Cs_2NaInCl_6$, as well as Fe^{3+} and Ag^+ co-doped DP denoted as Fe^{3+}-doped $Cs_2Ag_{0.5}Na_{0.5}InCl_6$ and Fe^{3+}-doped $Cs_2AgInCl_6$ DP NCs, respectively. They were labelled as $Cs_2NaInCl_6$: *y*% Fe, $Cs_2Ag_{0.5}Na_{0.5}InCl_6$: *y*% Fe, and $Cs_2AgInCl_6$: *y*% Fe, where *y*% (25% and 50%) is the molar ratio of the iron precursor relative to that of the indium precursor used during synthesis. It is important to note that the 25% and 50% are nominal amounts of Fe, which are very different from the actual amount of the incorporated Fe^{3+}-dopant, as will be discussed later on.

Crystal structure, morphology, and elemental composition

The crystal structure and phase purity of undoped, Fe^{3+}-doped, and Fe^{3+}/Ag^+ co-doped DP NCs were investigated by X-ray diffraction (XRD) measurements (Fig. 1a). All the observed diffraction peaks in both Fe^{3+}-doped and undoped samples match well with the corresponding bulk reflections of $Cs_2NaInCl_6$ and do not contain any impurities. Upon closer examination of the (044) diffraction peak (right panel in Fig. 1a), a noticeable shift towards a higher diffraction angle is observed after the incorporation of Fe^{3+} ions due to the lattice shrinkage. The observed lattice shrinkage can be attributed to the smaller ionic radius of Fe^{3+} (0.64 Å) compared to In^{3+} (0.81 Å), providing clear evidence of the successful incorporation of Fe^{3+} ions into the host DP structure.

Regarding Fe^{3+}/Ag^+ co-doped samples, XRD patterns of Fe^{3+}-doped $Cs_2Ag_{0.5}Na_{0.5}InCl_6$ (Fig. S2†) NCs show a similar trend and do not contain any impurity peaks, confirming the preservation of the cubic DP structure. The only exception is observed for 50% Fe-doped $Cs_2AgInCl_6$ NCs (Fig. S3†), where the synthesis does not yield pure phase NCs. This can be attributed to the distinct growth kinetics and some saturation limits in terms of the actual concentration of the iron ions doped into the host DP structure (as will also be discussed later).

The actual amount of the Fe^{3+}-dopant in $Cs_2Ag_{1-x}Na_xInCl_6$ ($x = 0, 0.5, 1$) NCs was retrieved by inductively coupled plasma mass spectrometry (ICP-MS) measurements. The ICP-MS results (Tables S1–S3†) reveal that the Fe amount present in the host DP significantly varies for different DP systems. The $Cs_2NaInCl_6$ NCs accommodated a maximum concentration of Fe while the lowest amount of Fe can be incorporated into $Cs_2AgInCl_6$, under similar reaction conditions. In particular, for a nominal 25% Fe feeding during the synthesis, the actual atomic concentrations of the Fe dopant (related to In) in $Cs_2NaInCl_6$, $Cs_2Ag_{0.5}Na_{0.5}InCl_6$, and $Cs_2AgInCl_6$ are 8.1%, 3.4% and 0.8%, respectively. Notably, the actual contents of Na in the $Cs_2Ag_{0.5}Na_{0.5}InCl_6$ DP NCs (Table S2†) are in close agreement with the amount of Na precursor that was used in the reaction.

Next, EPR measurements were performed at room temperature to gain insight on the spin state of iron in the host NCs. EPR spectra (Fig. 1b) of Fe^{3+}-doped (25% feeding concentration) $Cs_2Ag_xNa_{1-x}InCl_6$ ($x = 0$, 0.5 and 1) NCs show a strong resonance signal from all samples located at $g \sim 2.03$, ascribed to paramagnetic Fe^{3+} ions.[39] In contrast, EPR spectra (Fig. S4†) of undoped $Cs_2NaInCl_6$ NCs do not show any resonance signal in the probed range of magnetic fields. Thus, the absence of any resonance signal in the EPR spectrum of undoped $Cs_2NaInCl_6$ NCs clearly validates that the strong resonance signal in all Fe^{3+}-doped systems indeed originated from the presence of paramagnetic Fe^{3+} ions.

X-ray photoelectron spectroscopy (XPS) was performed to study the chemical composition of DP NCs. Full range survey and high-resolution XPS spectra for Cs 3d, Ag 3d, Na 1s, In 4d, Cl 3p and Fe 2p of iron doped (25% of Fe feeding with respect to In, which was hereafter used as the benchmark for all the following key measurements) $Cs_2Ag_{1-x}Na_xInCl_6$ ($x = 0, 0.5, 1$) NCs are shown in Fig. S5a–c and S6a–f,† respectively. The XPS spectra of Fe^{3+}-doped $Cs_2NaInCl_6$ NCs confirm the presence of all constituent elements in the expected oxidation states. However, in the XPS spectrum of Fe^{3+}-doped $Cs_2Ag_{0.5}Na_{0.5}InCl_6$ and $Cs_2AgInCl_6$, the presence of iron could not be verified, which may be due to the low concentration of Fe at the surface of the NC film which may be beyond the detection limit of XPS as previously reported by other research groups.[27,30,39]

The shape and size of the undoped and Fe^{3+}-doped $Cs_2Ag_xNa_{1-x}InCl_6$ ($x = 0$, 0.5 and 1) NCs were investigated by transmission electron microscopy (TEM). The TEM images of undoped (Fig. 1c, f and i) and 25% Fe^{3+} doped $Cs_2Ag_xNa_{1-x}InCl_6$ ($x = 0$, 0.5 and 1) NCs are presented in Fig. 1d, g and j. These images confirm the formation of uniform size NCs with a well-defined cubic morphology, and an average edge size of 8–12 nm. Notably, the cubic-shape morphology of doped NCs is still

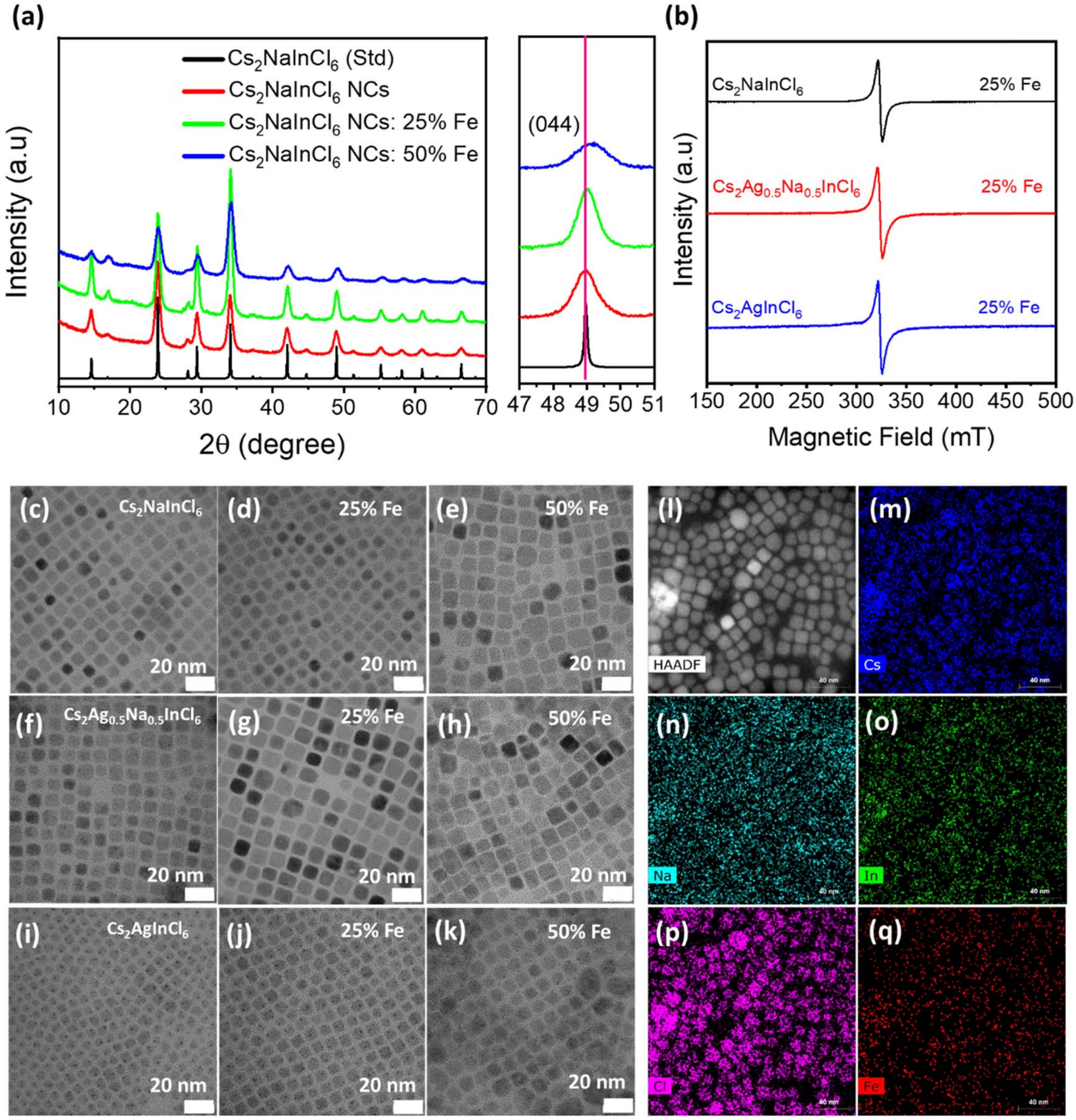

Fig. 1 (a) XRD patterns of undoped and Fe^{3+}-doped $Cs_2NaInCl_6$ NCs, with the corresponding reflections of bulk $Cs_2NaInCl_6$ (labeled as Std). The right panel shows an enlarged view of the (044) diffraction peaks of the DP samples. (b) EPR signals of Fe^{3+}-doped $Cs_2Ag_xNa_{1-x}InCl_6$ ($x = 0$, 0.5 and 1) NCs with a nominal 25% Fe amount, measured at room temperature. (c–k) TEM images of Fe^{3+}-doped $Cs_2Ag_xNa_{1-x}InCl_6$ ($x = 0$, 0.5 and 1) NCs. (l) High-angle annular dark-field (HAADF) image of Fe^{3+}-doped $Cs_2NaInCl_6$ NCs with a nominal iron concentration of 50% and (m–q) STEM-EDS elemental mapping of Cs, Na, In, Cl, and Fe elements which show their homogeneous distribution within the cubic NCs.

retained even for 50% Fe^{3+} doping. However, the size distribution becomes broader and, in the case of $Cs_2AgInCl_6$ NCs, larger aggregates of the NCs are clearly visible (Fig. 1e, h and k). The morphology and elemental analysis of $Cs_2NaIn_{0.5}Fe_{0.5}Cl_6$ NCs were also investigated by high-angle annular dark-field (HAADF) scanning TEM (STEM) imaging and STEM-energy dispersive X-ray spectroscopy (EDS) elemental mapping. The HAADF-STEM image (Fig. 1l) further confirms the cubic shape of $Cs_2NaIn_{0.5}Fe_{0.5}Cl_6$ NCs, while STEM-EDS elemental mapping (Fig. 1m–q) demonstrates a homogeneous distribution of Cs, Na, In, Cl and Fe elements across the $Cs_2NaIn_{0.5}Fe_{0.5}Cl_6$ NCs. Additionally, the high-resolution TEM (HRTEM) image and the corresponding fast Fourier transform (FFT) (inset) of a single $Cs_2NaInCl_6$ NC (Fig. S7a†) reveal high crystallinity with a lattice spacing of 0.372 nm, corresponding to the (220) crystal plane. In the Fe^{3+}-doped $Cs_2NaInCl_6$ NCs, the lattice spacing of the (220) plane slightly decreases to 0.370 nm and 0.367 nm for 25% and 50% Fe^{3+}-doped $Cs_2NaInCl_6$ NCs (Fig. S7a–c†), respectively. This is ascribed to the substitution of larger In^{3+} by smaller Fe^{3+} ions. The decrease in the lattice spacing is in agreement with the shift of the diffraction peak towards a higher diffraction angle in the XRD patterns (Fig. 1a). The decrease in the lattice spacing of Fe^{3+}-doped $Cs_2NaInCl_6$ NCs further corroborates the successful incorporation of Fe^{3+} ions. Similar trends were also observed in Fe^{3+}-doped $Cs_2Ag_{0.5}Na_{0.5}InCl_6$ NCs (Fig. S7d–f†).

Optical properties of undoped and Fe^{3+}-doped $Cs_2Ag_xNa_{1-x}InCl_6$ ($x = 0$, 0.5 and 1) NCs

To explore the effect of iron and silver co-doping on the optical properties of $Cs_2NaInCl_6$ DP NCs, we performed UV-vis absorbance, steady-state PL, and time-resolved PL measurements on both undoped and Fe-doped $Cs_2Ag_xNa_{1-x}InCl_6$ ($x = 0$, 0.5 and 1) NCs. As shown in Fig. 2a and e, both $Cs_2NaInCl_6$ and $Cs_2AgInCl_6$ NCs exhibit featureless absorption with the onset near 330 and 350 nm, respectively, in agreement with previous reports.[35,36] In contrast to this, $Cs_2Ag_{0.5}Na_{0.5}InCl_6$ NCs show a clear excitonic absorption peak (Fig. 2c) at 330 nm which is attributed to the breaking of the parity-forbidden transition upon partial Na substitution with Ag.[14] Interestingly, Fe^{3+}-doped $Cs_2NaInCl_6$ NCs (Fig. 2a) display a dramatic shift of the optical band edge reaching towards 505 nm, and consequently the colour of their colloidal solution (inset of Fig. 2a) turns from colourless to yellow. Tauc plots (Fig. 2b) show that the optical band gap decreased from 4.29 eV for the undoped $Cs_2NaInCl_6$ NCs to 2.88 eV for the 25% Fe doped $Cs_2NaInCl_6$ NCs, in agreement with recently reported bulk and single crystal Fe^{3+}-doped DP systems.[27,30] On the other hand, Fe^{3+}-doped $Cs_2AgInCl_6$ NCs (Fig. 2e) exhibit an obvious red-shift in the absorption edge, while in the case of Fe^{3+}-doped $Cs_2Ag_{0.5}Na_{0.5}InCl_6$ NCs (Fig. 2c) the absorption edge lies in between that of Fe^{3+}-doped $Cs_2NaInCl_6$ NCs and Fe^{3+}-doped $Cs_2AgInCl_6$ NCs, respectively.

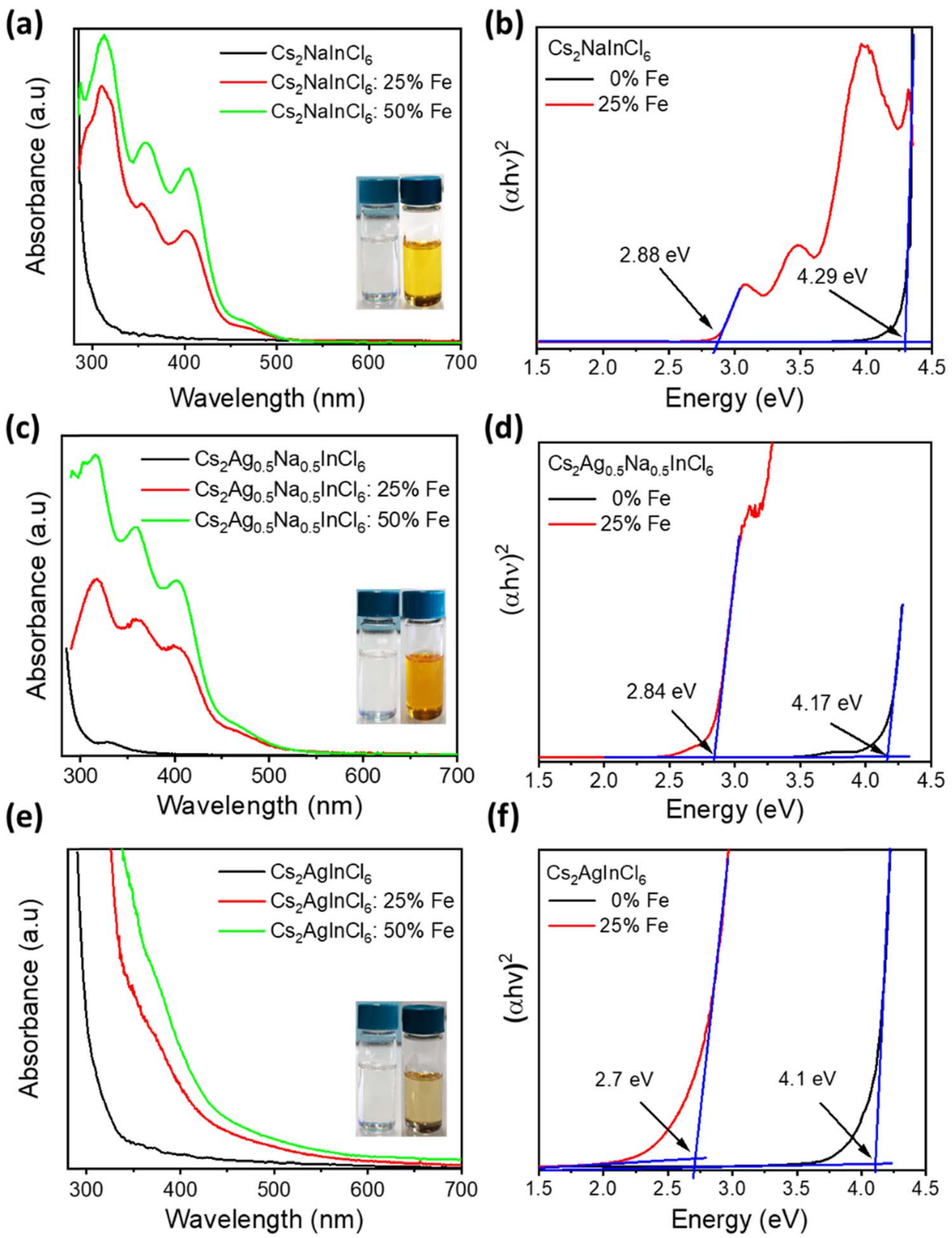

Fig. 2 UV-vis absorption spectra of undoped and Fe^{3+}-doped (a) $Cs_2NaInCl_6$, (c) $Cs_2Ag_{0.5}Na_{0.5}InCl_6$, and (e) $Cs_2AgInCl_6$ NCs, respectively. (Inset) Photographs of the undoped sample (left) and the Fe^{3+}-doped sample (right) with a nominal iron concentration of 25%. Tauc plots of undoped and Fe^{3+}-doped samples with a nominal iron concentration of 25%. (b) $Cs_2NaInCl_6$, (d) $Cs_2Ag_{0.5}Na_{0.5}InCl_6$, and (f) $Cs_2AgInCl_6$ NCs, respectively.

According to Tauc plots of $Cs_2AgInCl_6$ NCs and $Cs_2Ag_{0.5}Na_{0.5}InCl_6$ NCs, the band gap is reduced from 4.1 to 2.7 eV and from 4.17 to 2.84 eV upon Fe^{3+}-doping (Fig. 2f and d), respectively. We note that for all samples with nominal 50% Fe doping, the absorption intensity (Fig. 2a, c and e) increases, while the absorption onset and the band gap (Fig. S8a–c†) remain unchanged.

Fig. S9a† shows steady state PL spectra of undoped $Cs_2Ag_xNa_{1-x}InCl_6$ ($x = 0$, 0.5 and 1) NCs with different x values. The PL spectra of $Cs_2NaInCl_6$ NCs display a narrow emission band centered at 427 nm, while $Cs_2AgInCl_6$ NCs exhibit broadband emission with the PL maximum located at 580 nm. The PL signal of $Cs_2NaInCl_6$ NCs originates from defect related states, while the broadband emission from $Cs_2AgInCl_6$ NCs can be assigned to the emission *via* recombination of self-trapped excitons (STEs).[35,36] Both NCs and bulk DP materials commonly display a very week PL signal due to the presence of parity-forbidden transitions.[14] In the case of $Cs_2Ag_{0.5}Na_{0.5}InCl_6$ NCs, the intensity of the broadband emission is significantly enhanced compared to that of $Cs_2AgInCl_6$ NCs due to the breaking of parity-forbidden transitions upon partial Na alloying.[14] Upon nominal 25% Fe^{3+} doping, the PL spectra of $Cs_2Ag_xNa_{1-x}InCl_6$ ($x = 0$, 0.5 and 1) NCs exhibited distinct features compared to those of the respective undoped or exclusively Ag-alloyed counterparts. The PL spectra (Fig. S10a†) of Fe^{3+}-doped $Cs_2NaInCl_6$, $Cs_2Ag_{0.5}Na_{0.5}InCl_6$, and $Cs_2AgInCl_6$ NC solutions exhibit PL maxima at 455, 468, and 503 nm, respectively. It can be seen that the broadband features of STE emission from undoped samples have disappeared upon Fe doping, and a relatively sharp PL peak emerged in all samples. These results indicate that the observed PL signals from the Fe-doped samples do not originate from STEs but rather may result from recombination of free-excitons *via* sub-band gap states.[30]

Next, time-resolved PL (TRPL) measurements were carried out in order to understand the charge recombination dynamics of Fe-doped $Cs_2Ag_xNa_{1-x}InCl_6$ ($x = 0$, 0.5 and 1) NCs using the time correlated single photon counting technique. The TRPL spectra and their fitted kinetic parameters for all undoped and Fe-doped $Cs_2Ag_xNa_{1-x}InCl_6$ ($x = 0$, 0.5 and 1) NCs are presented in Fig. S9b, c, S10b and Tables S4, S5,† respectively. The TRPL spectra of $Cs_2NaInCl_6$ NCs (Fig. S9c†) reveal an average PL lifetime of 6.4 ns. On the other hand, both $Cs_2AgInCl_6$ and $Cs_2Ag_{0.5}Na_{0.5}InCl_6$ NCs (Fig. S9b†) exhibit a much longer PL lifetime of about 2.9 μs and 4.2 μs, respectively, as expected for STE emission.[14,35] The increase in PL intensity and PL lifetime of $Cs_2Ag_{0.5}Na_{0.5}InCl_6$ NCs can indeed be attributed to the improvement in radiative recombination of STEs enabled by breaking of parity-forbidden transitions upon Na-alloying into $Cs_2AgInCl_6$ NCs. Next, we analyzed the PL decay profiles of all Fe^{3+}-doped NCs (see extracted parameters in Table S5†), and found out average PL lifetimes of 6.2, 6.8, and 4.7 ns for Fe^{3+}-doped $Cs_2NaInCl_6$, $Cs_2Ag_{0.5}Na_{0.5}InCl_6$, and $Cs_2AgInCl_6$ NCs, respectively. All the Fe^{3+}-doped NCs exhibit fast recombination carrier dynamics relative to undoped samples, with nanosecond PL lifetimes, most likely because the STEs can effectively dissociate to free electrons and holes. These results suggest that iron and silver co-doping is advantageous in order to manipulate the optoelectronic properties of DP NCs for use as photoactive materials in solar cells or photocatalysis where specific energies of band levels as well as charge separation are required.

Analysis of the optical properties of iron and silver co-doped DPs by DFT calculations

To explain the optical properties of Fe-doped DP NCs, we used DFT calculations with the implementation of the Heyd, Scuseria, and Ernzerhof (HSE03) hybrid functional,[42,43] coupled with optical-transition calculations obtained by solving the Bethe–Salpeter equation (BSE)[44–46] (see Table S8 in the ESI†). The calculated optical band gap of 4.43 eV for pristine $Cs_8Na_4In_4Cl_{24}$ agrees well with the experimental data (4.29 eV). Fe-doping reduces the band gap to approximately 2.85–3.12 eV depending on the Fe^{3+} electronic configuration, but it remains insensitive to the Fe^{3+} feeding amount in the range of 25–50%. The degree of band gap reduction caused by Fe doping is influenced by the geometry and spin state of Fe. Fe^{3+} ions in a $3d^5$ valence configuration in an octahedral ligand field have either a high spin or a low spin state, while the actual spin state depends on the relative strengths of crystal field splitting and electron–electron repulsion. The high-spin isomer of Fe^{3+} ($t_{2g}^3e_g^2$) in the DP-NCs leads to better agreement with the experimental values (Table S8†). Fe^{3+} doping creates intra-gap states, which can occur in either both spin channels (in the low-spin configuration) or in the minority spin channel (in the high-spin configuration), as illustrated in Fig. S22.† The band structure shown in Fig. S23† reveals that these states are strongly localized on Fe atoms and remained nearly independent of the Fe doping amount. Experimental measurements have shown that substituting Ag for Na in pristine $Cs_8Na_4In_4Cl_{24}$ does not lead to a significant reduction of the band gap, which varies from 4.29 eV (undoped system) to 4.17 and 4.10 eV for $Cs_2Ag_{0.5}Na_{0.5}InCl_6$ and $Cs_2AgInCl_6$, respectively (Fig. 2b, d and f). A similar trend is observed in the DFT calculations, which suggests the strong impact of Ag alloying on the electronic structure of $Cs_8Na_4In_4Cl_{24}$ (Fig. S24 and S25†). As the degree of Ag incorporation increases, the electronic band gap narrows in a similar manner to the optical band gaps, resulting from the upshift/downshift of the valence/conduction band edges with each additional Ag^+ ion. Ag^+ ions, similar to Fe^{3+} ions, are situated within the octahedral ligand field of the six Cl atoms, which causes Ag^+ 4d orbital splitting into two energy levels: the lower energy t_{2g} and the higher-lying e_g. However, the states introduced by the Ag^+ dopant are unlikely to contribute to light absorption near the absorption edge, because the optical transition edge is located directly below the hybridized states of Ag and Cl. In contrast, the introduction of Fe^{3+} into $Cs_2AgInCl_6$ and $Cs_2Ag_{0.5}Na_{0.5}InCl_6$ significantly decreases the band gap to 2.93–3.28 eV, which is consistent with the experimental observations (Fig. 2). Furthermore, electronic structure calculations (Fig. 3) indicated that Ag doping results in an upshift of the valence band edge (VBE), primarily composed of Cl and Ag states (or Cl in the case of $Cs_2NaInCl_6$), as well as the conduction band edge (CBE), whose orbital composition depends on the

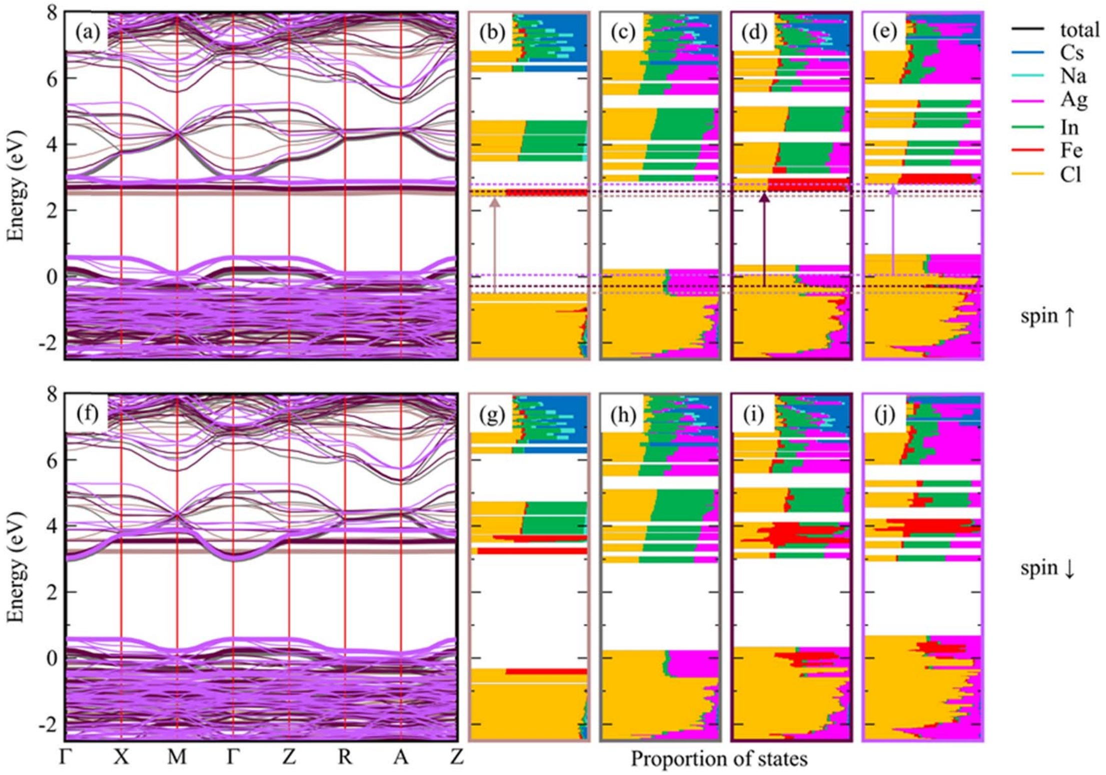

Fig. 3 Spin-resolved electronic band structure of optimized low-spin $Cs_8Na_4In_3Fe_1Cl_{24}$ with a constant In/Fe ratio, and the effect of Ag-doping on this system (a and f). The relaxed reference system without Fe, $Cs_8Na_2Ag_2In_4Fe_0Cl_{24}$, is also included for comparison. The colors in panels (a and f) conform to the bounding boxes of the corresponding DOS plots shown in (b–e and g–j), where the valence and conduction band edges are marked with bold lines. The DOS plots (see also Fig. S26†) of $Cs_8Na_4Ag_0In_3Fe_1Cl_{24}$ (b and g), $Cs_8Na_2Ag_2In_4Fe_0Cl_{24}$ (c and h), $Cs_8Na_2Ag_2In_3Fe_1Cl_{24}$ (d and i), and $Cs_8Na_0Ag_4In_3Fe_1Cl_{24}$ (e and j) are shown, and the transitions (corresponding to the optical band gap) are marked by arrows. The edges of these transitions are indicated by dashed horizontal lines. The electronic band structure and the DOS plots for the high-spin configuration of the same systems are presented in Fig. S27.†

spin channel. Specifically, for the spin-down channel, the CBE is formed by electronic states of Cl, In, and Ag, while for the spin-up channel, it is formed by Fe and less significantly by Cl. In $Cs_2NaInCl_6$, the VBE is contributed to by Cl and Fe in the spin-down channel, and by Cl in the spin-up channel, while the CBE is formed by Fe and Cl/Fe, respectively.

The analysis of the band gap and the atom-resolved density of states (DOS) shown in Fig. 3 leads to the conclusion that the optical transitions do not occur from the VBEs but instead from the Cl states located directly below the hybridized Ag and Cl VBE states. This same conclusion can be drawn for the high-spin configurations of the same system (Fig. S27†). The transition leads to the d-orbitals of Fe atoms, which is crucial for the photocatalysis of CO_2 reduction as will be thoroughly discussed below.

Stability of Fe^{3+}-doped $Cs_2Ag_xNa_{1-x}InCl_6$ ($x = 0$, 0.5 and 1) NCs

Ensuring the long-term material stability of DP NCs is of utmost importance for their practical applications. We conducted a thorough examination of long-term colloidal, structural, and morphological stability of Fe^{3+}-doped $Cs_2Ag_xNa_{1-x}InCl_6$ ($x = 0$, 0.5 and 1) NCs. In our case, the extensively washed Fe^{3+} (with a nominal 25% Fe amount) doped $Cs_2Ag_xNa_{1-x}InCl_6$ ($x = 0$, 0.5, and 1) NCs, displayed remarkable long-term colloidal, structural, and morphological stability when stored under ambient conditions. The photographs of both fresh and aged samples of Fe^{3+}-doped (25% Fe) $Cs_2Ag_xNa_{1-x}InCl_6$ ($x = 0$, 0.5, and 1) NCs, presented in the insets of Fig. S11a, S12a and S13a† show no signs of sedimentation; they appear identical even after 30 days of storage under ambient conditions. Furthermore, the absorption spectra (Fig. S11a, S12a and S13a†) of both fresh and aged Fe^{3+}-doped $Cs_2Ag_xNa_{1-x}InCl_6$ ($x = 0$, 0.5, and 1) NCs remain unchanged, indicating consistent optical properties over the storage period. The XRD patterns (Fig. S11b, S12b and S13b†) of the aged samples also exhibit minimal changes, attested to the sustained structural integrity of the NCs during storage under ambient conditions. Additionally, the TEM images (Fig. S11c, S12c and S13c†) of the aged Fe^{3+}-doped $Cs_2Ag_xNa_{1-x}InCl_6$ ($x = 0$, 0.5, and 1) NCs reveal their preserved cubic morphology, devoid of any signs of aggregation or degradation. This provides further evidence of their exceptional long-term structural stability. However, Fe^{3+}-doped $Cs_2Ag_xNa_{1-x}InCl_6$ ($x = 0.5$ and 1) NCs synthesized with a 50% Fe^{3+} loading exhibited relatively poor colloidal stability. Specifically, in the case of Fe^{3+}-doped $Cs_2Ag_{0.5}Na_{0.5}InCl_6$ NCs, a small amount of yellow-orange precipitate was observed at the bottom of the vial after 30 days of storage under ambient conditions (inset of Fig. S12d†). Despite this sedimentation, the shape of the absorption spectra (Fig. S11d and S12d†), crystal structure (Fig. S11e and S12e†), and cubic morphology (Fig. S11f and S12f†) of both Fe^{3+}-doped $Cs_2NaInCl_6$ and $Cs_2Ag_{0.5}Na_{0.5}InCl_6$ NCs, synthesized with a 50% Fe^{3+} loading, remained preserved. In contrast, Fe^{3+}-doped $Cs_2AgInCl_6$ NCs synthesized with a 50% Fe^{3+} loading exhibited poor colloidal and structural stability, as evidenced by complete precipitation at the bottom of the vial within a few days of storage under ambient conditions (inset of Fig. S13d†). This instability in Fe^{3+}-doped $Cs_2AgInCl_6$ NCs with a 50% nominal Fe^{3+} loading is also reflected in their irregular morphology (Fig. S13f†) along with the presence of impurity phases (Fig. S13e†), which likely resulted in poorly capped NCs. Overall, the colloidal and structural stability of Fe^{3+}-doped $Cs_2Ag_xNa_{1-x}InCl_6$ ($x = 0.5$ and 1) NCs varied depending on the Fe^{3+} loading, with the 50% nominal Fe^{3+} loading showing adverse effects on the stability of $Cs_2Ag_{0.5}Na_{0.5}InCl_6$ and $Cs_2AgInCl_6$ NCs, but not significantly affecting $Cs_2NaInCl_6$ NCs. These findings underscore the importance of carefully optimizing the doping concentration to achieve the desired stability and performance of these NCs in potential optoelectronic applications.

Surface chemistry

Next, our investigation delved deeper into understanding the factors contributing to the remarkable stability observed in extensively washed Fe^{3+}-doped DP NCs. It is widely recognized that the binding of capping ligands to the surface of colloidal NCs plays a pivotal role in achieving high-quality products with high colloidal and structural stability during the extraction and purification process. Given the uniform shape and size, as well as the colloidal and structural stability observed in both fresh and aged samples, we hypothesized that the superior quality and stability of the DP NCs could be attributed to efficient surface passivation through robust surface capping ligands. To research the surface chemistry and nature of ligands bound to the surface of iron-doped DP NCs, we conducted ^1H and ^{31}P nuclear magnetic resonance (NMR) measurements. Fig. S14a† displays the ^1H NMR spectra of extensively washed Fe^{3+} (with a 25% nominal Fe^{3+} loading) doped $Cs_2Ag_{0.5}Na_{0.5}InCl_6$ NCs, showing several broad signals corresponding to bound ligands and characteristic sharp signals from the solvents used during the purification process and for dispersing the DP NCs. Importantly, the extensively washed NCs showed no sharp signals from unwanted organic residues, such as unbound ligands and octadecene. However, the intense and broad signals at 5.53 ppm from alkene protons of OA and/or OLA remained preserved, suggesting that either OLA or OA, or both are strongly bound to the surface of the NCs. Furthermore, the NMR spectra revealed the presence of characteristic broad peaks of oleylammonium ions at 7.5 and 4.1 ppm, corresponding to the α-proton ($-NH^{3+}$) and β-proton nearest to the amine group (CH_2–N), respectively, which verifies the binding of OLA to the NC surface. Additionally, the presence of a broad peak at 2.2 ppm corresponding to the proton (1) of OA, which is unique for OA, further supports the binding of OA to the NC surface. Hence, the presence of broad peaks from alkene protons along with the unique peaks of both OLA and OA in extensively washed samples clearly demonstrates that both oleylammonium and oleate ligands are bound together to the surface of the NCs. According to our previous reports on TOP-based synthesis of DP NCs, the *in situ* generated phosphonium species, which can be formed by a nucleophilic reaction between TOP and benzoyl chloride, serve as highly reactive halide sources and surface capping ligands.[35,36] To further investigate the possible binding of phosphonium cations to the surface of iron-doped DP NCs, we performed ^{31}P NMR spectroscopy measurements. The ^{31}P NMR spectra (Fig. S14b†) of extensively washed NCs exhibited a broad signal at 35.2 ppm, accompanied by a small peak at 10.2 ppm, which correspond to benzoyl trioctylphosphonium and trioctylphosphonium cations, respectively.[36] Moreover, the broadened peaks at 35.2 ppm and 10.2 ppm in the ^{31}P NMR spectra (Fig. S14b†), along with the broadened peak of aromatic protons from the benzoyl group at 8.2 ppm in the ^1H NMR spectra (Fig. S14a†), suggest the binding of benzoyl trioctylphosphonium and trioctylphosphonium cations at the Cl sites of the iron-doped DP NCs. Thus, NMR results confirm that the extensively washed iron-doped DP NCs are effectively passivated by robust cationic ligands, such as oleylammonium and phosphonium species, together with oleate anions. This combined surface passivation approach contributes to the high colloidal and structural stability observed in extensively washed Fe^{3+}-doped DP NCs.

Photocatalytic CO_2 reduction

The combination of a suitable band gap and exceptional material stability in Fe-doped $Cs_2AgInCl_6$, $Cs_2NaInCl_6$, and $Cs_2Ag_{0.5}Na_{0.5}InCl_6$ DP NCs has sparked our interest in exploring their potential for photocatalytic CO_2 reduction. The reactions were carried out in a CO_2 saturated ethyl acetate/isopropanol solvent mixture under simulated solar light illumination with an intensity of 150 mW cm^{-2} (AM 1.5G). Ethyl acetate was chosen as the reaction medium due to high solubility of CO_2 and excellent stability of DP NCs in this solvent, while isopropanol served as a hole scavenger and a proton source.[47,48] We started from the comparison of the photocatalytic activity of nominal 25% Fe-doped DP NCs. Notably, although the detected photocatalytic CO_2 reduction products were CH_4 and CO for all the tested photocatalysts, we registered a marked difference in both the product yield and selectivity (Fig. 4a). In particular, Fe^{3+}-doped $Cs_2Ag_{0.5}Na_{0.5}InCl_6$ DP NCs offer the highest activity with a CH_4 yield of 18.3 μmol g^{-1} and CO yield of 1.1 μmol g^{-1}, with a remarkable selectivity toward CH_4 formation. In addition, as compared to the recently reported photocatalysts based on lead-free perovskites for CO_2 reduction (Table S6, ESI†), Fe^{3+}-doped $Cs_2Ag_{0.5}Na_{0.5}InCl_6$ NCs show comparable performance to most of them towards solar-light-driven CO_2 reduction to CH_4. To validate the role of Fe^{3+}-doped $Cs_2Ag_{0.5}Na_{0.5}InCl_6$ NCs in photocatalytic CO_2 reduction into CH_4 and CO products, three control experiments (Fig. S15a†) were conducted under different experimental conditions. The first and second control

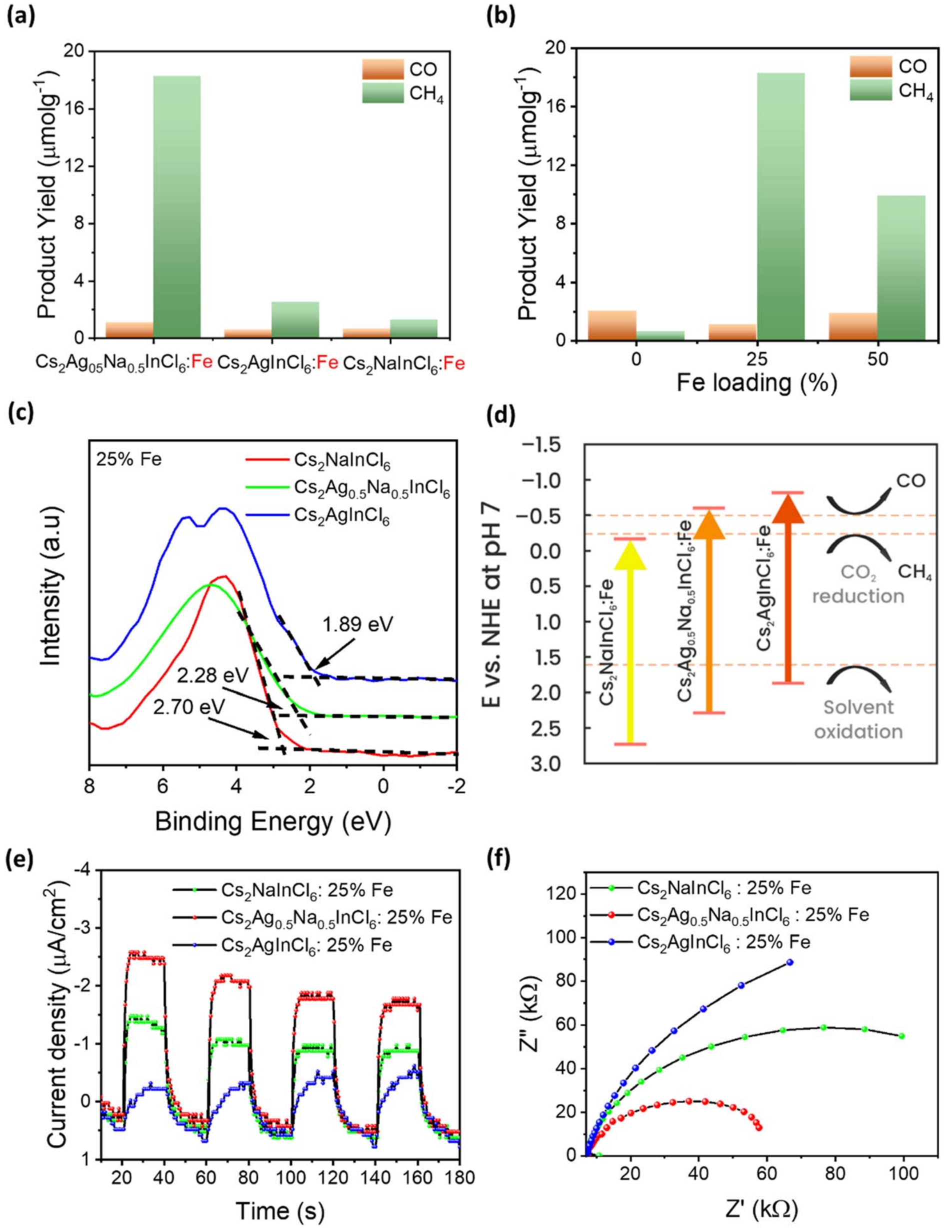

Fig. 4 (a) Comparison of photocatalytic CO_2 reduction performances after a 6 h reaction of Fe^{3+}-doped $Cs_2Ag_{0.5}Na_{0.5}InCl_6$, $Cs_2AgInCl_6$, and $Cs_2NaInCl_6$ NCs with a nominal iron concentration of 25%. (b) Product yield of the $Cs_2Ag_{0.5}Na_{0.5}InCl_6$ NCs with various nominal amounts of Fe^{3+} (with respect to In) from photocatalytic CO_2 reduction after 6 h of the reaction. (c) Valence band XPS spectrum and (d) schematic illustration of the energy band structures of Fe^{3+}-doped $Cs_2NaInCl_6$, $Cs_2Ag_{0.5}Na_{0.5}InCl_6$, and $Cs_2AgInCl_6$ NCs with a nominal iron concentration of 25%, respectively. The energy band structures were constructed on the basis of UV-vis and VB XPS results. (e) Transient photocurrent response recorded at $-0.4\ V_{Ag/AgCl}$ under chopped AM 1.5G illumination. (f) Nyquist plots obtained under illumination with a light intensity of 150 mW cm^{-2} at a bias of $-0.4\ V_{Ag/AgCl}$.

experiments were performed without light (in the dark) and without a catalyst, respectively, and no hydrocarbon products were detected, indicating that the presence of both light irradiation and a photocatalyst is essential for CO_2 reduction. The third control experiment was conducted similar to the standard photocatalytic CO_2 reduction but under an argon atmosphere instead of CO_2. The result shows (Fig. S15a†) that an insignificant amount of products was detected, which could be originated from the partial photooxidation of ethyl acetate and/or residual organic ligands bound to the surface of NCs, which is in agreement with the previous studies reported for perovskite NC based CO_2 reduction by several groups.[13,48–53] Additionally, the products of photocatalytic CO_2 reduction were further verified by an isotope labelling experiment. As shown in Fig. S15b,† following the photocatalytic reaction in a $^{13}CO_2$ atmosphere, the mass spectra revealed a major signal of $^{13}CH_4$ ($m/z = 17$) and a trace of ^{13}CO ($m/z = 29$). These results affirm that the CH_4 indeed originated from the photocatalytic reduction of CO_2 over the photocatalyst. On the other hand, Fe^{3+}-doped $Cs_2AgInCl_6$ and $Cs_2NaInCl_6$ NCs demonstrate much lower catalytic performance, resulting in a CH_4 yield of 2.52 and 1.28 μmol g^{-1}, respectively. Undoped $Cs_2Ag_{0.5}Na_{0.5}InCl_6$ NCs (Fig. 4b) produce only a trace amount of CH_4 (0.61 μmol g^{-1}) and CO (2.02 μmol g^{-1}) products. The poor photocatalytic performance of the undoped sample is attributed to the large band gap (4.17 eV) and thus poor light absorption capabilities. In contrast, 50% nominal Fe^{3+}-doped $Cs_2Ag_{0.5}Na_{0.5}InCl_6$ NCs were significantly active but lower (Fig. 4b) in comparison with the 25% nominal Fe^{3+}-doped sample, probably due to their poor quality and stability (see stability discussion in the ESI†). Thus, our results demonstrate that Fe^{3+} doping not only improves the light absorption capability of DP NCs but also regulates their photocatalytic performance towards selective reduction of CO_2 into CH_4. Moreover, to investigate the stability of the Fe^{3+}-doped $Cs_2Ag_{0.5}Na_{0.5}InCl_6$ NCs, a cyclic experiment was carried out under similar reaction conditions. As shown in Fig. S16,† no obvious decay of the product yield was observed after three cycles of repeated photocatalytic reaction. Remarkably, both the double perovskite crystal structure (Fig. S17a†) and the cubic morphology (Fig. S17b†) of Fe^{3+}-doped $Cs_2Ag_{0.5}Na_{0.5}InCl_6$ NCs are preserved after the photocatalytic reaction, demonstrating superior material stability.

To explore the reasons for the different performances of photocatalytic CO_2 reduction, we analysed the energy band alignment and band gap of Fe-doped $Cs_2NaInCl_6$, $Cs_2Ag_{0.5}Na_{0.5}InCl_6$, and $Cs_2AgInCl_6$ NCs. The XPS valence band (VB) edges *versus* Fermi level of nominal 25% Fe^{3+}-doped $Cs_2NaInCl_6$, $Cs_2Ag_{0.5}Na_{0.5}InCl_6$, and $Cs_2AgInCl_6$ NCs is located at 2.70, 2.28, and 1.89 eV, respectively (Fig. 4c). The optical band gap of the Fe^{3+}-doped NCs calculated from the Tauc plots is 2.88, 2.84 and 2.70 eV, respectively. The corresponding conduction band (CB) positions are calculated using the equation $E_{CB} = E_{VB} - E_g$ and on the basis of these values, their band energy alignment with respect to the CH_4 and CO redox potentials is plotted in Fig. 4d. The CB position of Fe^3-doped $Cs_2NaInCl_6$ NCs is located at −0.18 eV, which makes it energetically unfavourable for CO_2 reduction, thus explaining the poor photocatalytic activity of this material. On the other hand, although Fe^{3+}-doped $Cs_2AgInCl_6$ NCs show favourable CB positions for the formation of both CH_4 and CO, the poor light absorption capabilities in the visible region could be the reason resulting in their poor performance. The strong light absorption in the visible region along with the suitable CB position of Fe^{3+}-doped $Cs_2Ag_{0.5}Na_{0.5}InCl_6$ NCs make them efficient for selective photocatalytic CO_2 reduction. DFT calculations (Fig. 3) show that Ag doping induces an upshift of the edges of optical transitions. The CB edges are primarily formed by the localized Fe states, whose positions are influenced by the level of Ag doping. The VB states formed by Ag and Cl states do not participate in the optical transition, and the edge is placed directly below these states. With increasing doping, the CB edge shifts up along with the optical transition edges, resulting in the band gap remaining nearly unchanged. Besides electronic arguments, therefore, the simultaneous presence of Na, Ag, and Fe, *i.e.* the NC chemical composition, is crucial to facilitate the activation of CO_2 and its transformation into CH_4.

In order to further probe the enhanced photocatalytic CO_2 reduction ability of Fe^{3+}-doped $Cs_2Ag_{0.5}Na_{0.5}InCl_6$ NCs, CO_2 adsorption/desorption measurements were performed. The CO_2 adsorption/desorption isotherms are shown in Fig. S18.† It can be seen that Fe^{3+}-doped $Cs_2Ag_{0.5}Na_{0.5}InCl_6$ NCs exhibit higher CO_2 adsorption capacity (5.1 cm^3 g^{-1}) than undoped $Cs_2Ag_{0.5}Na_{0.5}InCl_6$ NCs (2.9 cm^3 g^{-1}). The enhanced CO_2 adsorption by Fe^{3+}-doped $Cs_2Ag_{0.5}Na_{0.5}InCl_6$ NCs could be possibly assigned to the presence of extra adsorption sites induced by interstitial iron dopants. According to the previous reports, CO_2 molecules generally adsorb on the metal centres of perovskite materials,[54] and thus the introduction of iron dopants would manipulate the active sites for CO_2 adsorption and iron could act as active adsorption sites along with other metal ions. Next, photoelectrochemical characterization studies were performed to investigate the photogenerated charge separation and transfer behaviour of the three photocatalysts. The transient photoresponse curve shown in Fig. 4e demonstrated that the photocurrent of the samples was repeatable. In comparison to the Fe^{3+}-doped $Cs_2NaInCl_6$ and $Cs_2AgInCl_6$ NCs, the Fe^{3+}-doped $Cs_2Ag_{0.5}Na_{0.5}InCl_6$ NCs show significantly higher photocurrent density, indicating efficient separation of photogenerated charge carriers. Furthermore, the interfacial charge transfer resistance of the three catalysts was investigated by using electrochemical impedance spectra. The Nyquist plot (Fig. 4f) of Fe^{3+}-doped $Cs_2Ag_{0.5}Na_{0.5}InCl_6$ NCs has a smaller radius than that of Fe^{3+}-doped $Cs_2NaInCl_6$ and $Cs_2AgInCl_6$ NCs, implying a lower interfacial charge transfer resistance in Fe^{3+}-doped $Cs_2Ag_{0.5}Na_{0.5}InCl_6$ NCs. Thus electrochemical analysis clearly demonstrates the efficient separation and transfer of photogenerated charge carriers in Fe^{3+}-doped $Cs_2Ag_{0.5}Na_{0.5}InCl_6$ NCs which further validates their efficient photocatalytic activity.

To shed more light on the mechanism behind the selective reduction of CO_2 to CH_4, a computational analysis of the possible reaction pathway on (Fe^{3+}-doped) $Cs_8Na_2Ag_2In_3Fe_1Cl_{24}$ has been conducted and compared to that of the undoped system $Cs_8Na_2Ag_2In_4Fe_0Cl_{24}$. The energy profile, expressed in terms of the change in Gibbs energy, is illustrated in Fig. 5a. For the Fe^{3+}-doped system, the reaction initiates with the adsorption of a CO_2 molecule at the Fe^{3+} ion, followed by the successive addition of H atoms, and the removal of the resulting H_2O by-product. The change in Gibbs free energy (ΔG) of $*CO_2$ formation for an iron-doped system is lower than that of the undoped counterpart, implying that CO_2 adsorption and activation on the surface of an Fe^{3+}-doped system is more favourable compared to that of the undoped system (Fig. S28†). Moreover, the transformation of adsorbed CO_2 ($*CO_2$) into OCOH* on the Fe^{3+}-doped surface is an easy step and requires a small energy barrier of 0.08 eV. This could be attributed to the stronger binding of OCOH* through an interaction with the surface Fe atom. In particular, the formation energy of OCOH* is 2.29 eV for the undoped surface, which is much higher than that of the Fe^{3+}-doped surface ($\Delta G = -0.21$ eV). Thus, our result indicates that the hydrogenation of $*CO_2$ to the OCOH* intermediate is much easier on the Fe^{3+}-doped surface. However,

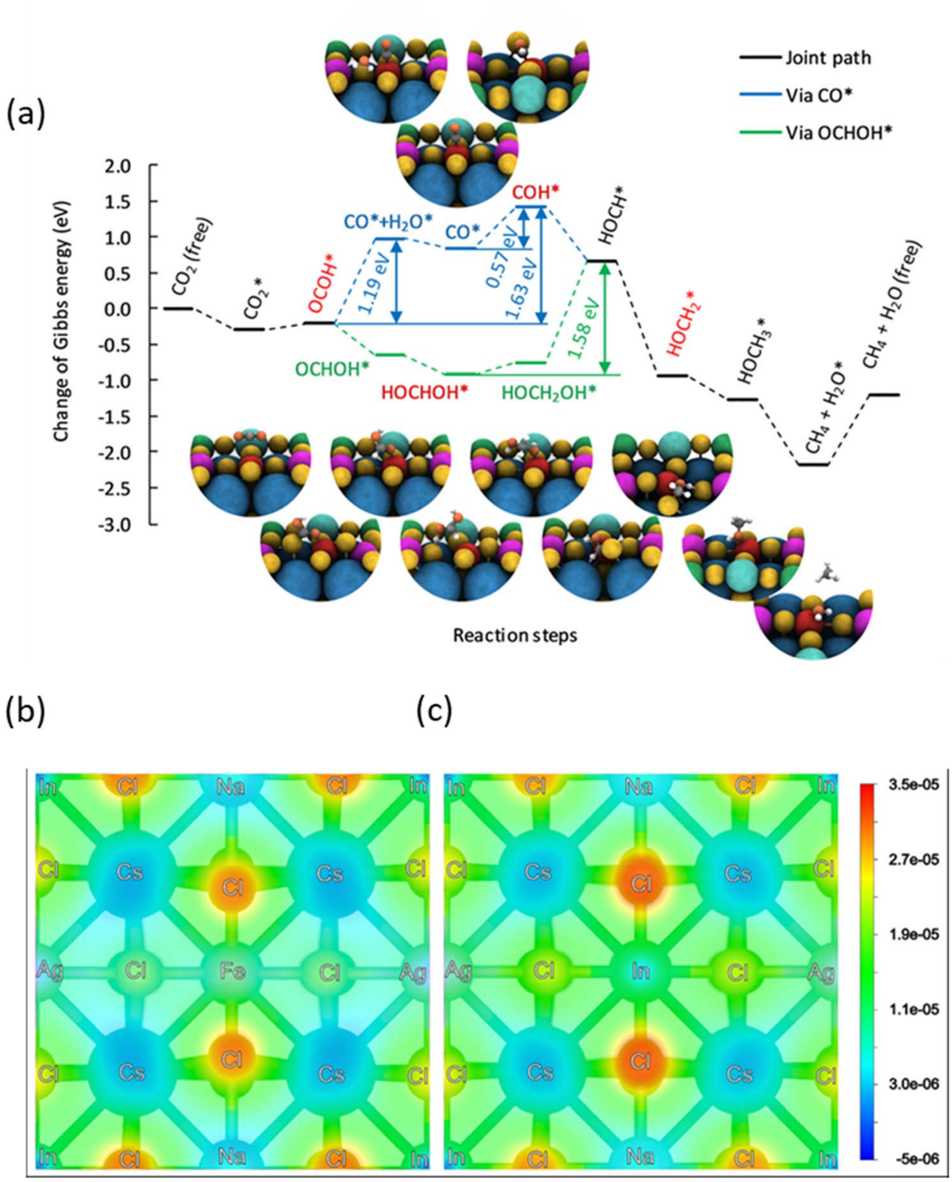

Fig. 5 (a) Energy profile for the reduction of CO_2 at a Fe^{3+} ion located on $Cs_8Na_2Ag_2In_3Fe_1Cl_{24}$, with each value calculated using a step-by-step procedure within the hybrid-DFT framework including the DFT-D3 vdW correction described in Computational methods (ESI).† The Gibbs energies are relative to the Gibbs energy of a free CO_2 molecule and free surface. For comparison on the $Cs_8Na_2Ag_2In_4Fe_0Cl_{24}$ surface, see Fig. S28.† Charge density plot of (b) Fe-doped and (c) pristine $Cs_4NaAgIn_2Cl_6$ surfaces corresponding to a CO_2 adsorption distance of 3.9 Å above the surfaces. Slightly negative values are caused by integrations within the PAW spheres.

protonation of OCOH* and conversion into *CO is an endothermic process that requires an energy input to overcome the barrier of 1.19 eV. In contrast, downhill free energy profiles of the continuous protonation of OCOH* intermediates suggest that conversion of OCOH* to OCHOH* is an exothermic reaction which could further drive the continuous protonation of CO_2. Nevertheless, the formation of HOCH* intermediates is the rate-limiting step for further protonation processes, but the hydrogenation of HOCH* to $HOCH_2^*$ and finally to CH_4 is thermodynamically spontaneous. According to the previous reports,[55–59] the selective reduction of CO_2 into CH_4 generally proceeds on the catalyst surface through a series of proton-coupled photogenerated electron transfer processes *via* the formation of several key intermediates such as OCOH*, HCO* and $HOCH_2^*$. The ΔG value of two key intermediates (OCOH*, and $HOCH_2^*$) for selective conversion of CO_2 to CH_4 over an Fe^3-doped surface is −0.21 eV for OCOH* and −0.93 eV for $HOCH_2^*$ which is substantially lower than that over the undoped surface (2.29 eV for OCOH* and 1.43 eV for $HOCH_2^*$). In general, lowering the free energy of key intermediates can concurrently reduce the activation energy barrier of the reaction, thereby enhancing the efficiency of CO_2 reduction. Moreover, the calculated charge distribution at a CO_2 adsorption distance of 3.9 Å above the surfaces (Fig. 5b and c) reveals only a slight difference in the vicinity of the Fe dopant, with a smaller gradient between Fe and Cl than that in the undoped surface.

Consequently, CO_2 tends to adsorb parallel to the surface on an Fe-doped system, favouring a slightly lower charged underlying atom for bonding. However, the change in Gibbs energy along the reaction profile shown in Fig. 5a indicates that the stabilization of the first intermediate in the subsequent steps is of greater significance. The results of DFT calculations clearly demonstrate that the Fe^3-doped surface dramatically improves CO_2 adsorption and activation, reducing the barrier for the formation of key intermediates for selective reduction of CO_2 to CH_4.

Conclusions

In summary, we successfully synthesised a series of Fe^{3+}-doped and Fe^{3+}/Ag^+ co-doped lead-free DP NCs. The incorporation of iron into $Cs_2NaInCl_6$ NCs results in extended visible light absorption, broadening the absorption edge from 330 nm to 505 nm, and reducing the band gap from 4.29 eV to 2.88 eV. The resulting absorption spectra are characterized by strong excitonic optical transitions. The presence of Fe and Ag, Na co-alloying enables a proper band energy alignment with the redox potential energy levels of CO and CH_4 produced during photocatalytic CO_2 reduction. This results in a stable and optimized photocatalyst (Fe-doped $Cs_2Ag_{0.5}Na_{0.5}InCl_6$) showing 94% methane selectivity for the reduction of CO_2. Our findings open up a reliable pathway to enhance the light absorption properties of lead-free DP NCs and to tune their band energy alignment and surface chemistry for selective photocatalytic reactions. Furthermore, our synthetic methodology holds great potential for the development of stable and lead-free light absorber materials for solution-processed photovoltaic and optoelectronic applications.

Data availability

The authors confirm that the data supporting the findings of this study are available within the article [and/or] its ESI.†

Conflicts of interest

There are no conflicts to declare.

Acknowledgements

RA and SK gratefully acknowledge support by the Czech Science Foundation, project GA CR 23-07971S. The work was further supported by the project Operational Programme Research, Development and Education – European Regional Development Fund, Project No. CZ.02.1.01/0.0/0.0/15_003/0000416 of the Ministry of Education, Youth and Sports of the Czech Republic, and by the Croucher Foundation of Hong Kong. RZ and SK acknowledge the funding from the Czech Science Foundation, project GA CR – EXPRO, 19-27454X. This work was also supported by the experimental and theoretical studies of near-infrared-emitting and chiral carbon dot luminophores project – from Moravian-Silesian Region, contract no. 00734/2023/RRC and European Union under the REFRESH – Research Excellence for Region Sustainability. The authors would also like to acknowledge High-tech Industries project number CZ.10.03.01/00/22_003/0000048 *via* the Operational Programme and ERDF/ESF project TECHSCALE (CZ.02.01.01/00/22_008/0004587). The IT4Innovations National Supercomputing Center is gratefully acknowledged for providing generous computational resources supported by the Ministry of Education, Youth and Sports of the Czech Republic through the e-INFRA CZ (No. 90254). JN acknowledges support by Palacký University Olomouc (project IGA_PrF_2024_017). LZ acknowledges the support from the Horizon Europe project HORIZON-WIDERA-2022-TALENTS "APPROACH" (No. 101120397).

References

1 Z. Xiao, Z. Song and Y. Yan, *Adv. Mater.*, 2019, **31**, 1803792.
2 H. Min, D. Y. Lee, J. Kim, G. Kim, K. S. Lee, J. Kim, M. J. Paik, Y. K. Kim, K. S. Kim, M. G. Kim, T. J. Shin and S. Il Seok, *Nature*, 2021, **598**, 444–450.
3 Y.-H. Kim, S. Kim, A. Kakekhani, J. Park, J. Park, Y.-H. Lee, H. Xu, S. Nagane, R. B. Wexler, D.-H. Kim, S. H. Jo, L. Martínez-Sarti, P. Tan, A. Sadhanala, G.-S. Park, Y.-W. Kim, B. Hu, H. J. Bolink, S. Yoo, R. H. Friend, A. M. Rappe and T.-W. Lee, *Nat. Photonics*, 2021, **15**, 148–155.
4 A. Swarnkar, V. K. Ravi and A. Nag, *ACS Energy Lett.*, 2017, **2**, 1089–1098.
5 T. C. Jellicoe, J. M. Richter, H. F. J. Glass, M. Tabachnyk, R. Brady, S. E. Dutton, A. Rao, R. H. Friend, D. Credgington, N. C. Greenham and M. L. Böhm, *J. Am. Chem. Soc.*, 2016, **138**, 2941–2944.
6 C. C. Stoumpos, L. Frazer, D. J. Clark, Y. S. Kim, S. H. Rhim, A. J. Freeman, J. B. Ketterson, J. I. Jang and M. G. Kanatzidis, *J. Am. Chem. Soc.*, 2015, **137**, 6804–6819.
7 B.-W. Park, B. Philippe, X. Zhang, H. Rensmo, G. Boschloo and E. M. J. Johansson, *Adv. Mater.*, 2015, **27**, 6806–6813.
8 B. Saparov, F. Hong, J.-P. Sun, H.-S. Duan, W. Meng, S. Cameron, I. G. Hill, Y. Yan and D. B. Mitzi, *Chem. Mater.*, 2015, **27**, 5622–5632.
9 A. H. Slavney, T. Hu, A. M. Lindenberg and H. I. Karunadasa, *J. Am. Chem. Soc.*, 2016, **138**, 2138–2141.
10 G. Volonakis, M. R. Filip, A. A. Haghighirad, N. Sakai, B. Wenger, H. J. Snaith and F. Giustino, *J. Phys. Chem. Lett.*, 2016, **7**, 1254–1259.
11 J. Zhou, Z. Xia, M. S. Molokeev, X. Zhang, D. Peng and Q. Liu, *J. Mater. Chem. A*, 2017, **5**, 15031–15037.
12 E. Greul, M. L. Petrus, A. Binek, P. Docampo and T. Bein, *J. Mater. Chem. A*, 2017, **5**, 19972–19981.
13 L. Zhou, Y.-F. Xu, B.-X. Chen, D.-B. Kuang and C.-Y. Su, *Small*, 2018, **14**, 1703762.
14 J. Luo, X. Wang, S. Li, J. Liu, Y. Guo, G. Niu, L. Yao, Y. Fu, L. Gao, Q. Dong, C. Zhao, M. Leng, F. Ma, W. Liang, L. Wang, S. Jin, J. Han, L. Zhang, J. Etheridge, J. Wang, Y. Yan, E. H. Sargent and J. Tang, *Nature*, 2018, **563**, 541–545.
15 L. Zdražil, S. Kalytchuk, M. Langer, R. Ahmad, J. Pospíšil, O. Zmeškal, M. Altomare, A. Osvet, R. Zbořil, P. Schmuki, C. J. Brabec, M. Otyepka and Š. Kment, *ACS Appl. Energy Mater.*, 2021, **4**, 6445–6453.

16 W. Zhu, W. Ma, Y. Su, Z. Chen, X. Chen, Y. Ma, L. Bai, W. Xiao, T. Liu, H. Zhu, X. Liu, H. Liu, X. Liu and Y. Yang, *Light: Sci. Appl.*, 2020, **9**, 112.

17 Z. Dong, S. Su, Z. Zhang, Y. Jiang and J. Xu, *Inorg. Chem.*, 2023, **62**, 1752–1761.

18 Z. Zhang, Q. Sun, Y. Lu, F. Lu, X. Mu, S.-H. Wei and M. Sui, *Nat. Commun.*, 2022, **13**, 3397.

19 R. Ahmad, G. V. Nutan, D. Singh, G. Gupta, U. Soni, S. Sapra and R. Srivastava, *Nano Res.*, 2021, **14**, 1126–1134.

20 Y. Jiang, K. Li, X. Wu, M. Zhu, H. Zhang, K. Zhang, Y. Wang, K. P. Loh, Y. Shi and Q.-H. Xu, *ACS Appl. Mater. Interfaces*, 2021, **13**, 10037–10046.

21 S. Kumar, I. Hassan, M. Regue, S. Gonzalez-Carrero, E. Rattner, M. A. Isaacs and S. Eslava, *J. Mater. Chem. A*, 2021, **9**, 12179–12187.

22 M. Yu, N. Wang, K. Lin, D. Song, J. Chen, T. Liang, J. Sun, K. Pan and H. Fu, *J. Mater. Chem. A*, 2023, **11**, 4302–4309.

23 K. Du, W. Meng, X. Wang, Y. Yan and D. B. Mitzi, *Angew. Chem.*, 2017, **129**, 8270–8274.

24 Y. Liu, P. Jain, I. J. Cleveland, M. Tran, S. Sarp, K. Sandrakumar, R. S. Rodriguez and E. S. Aydil, *J. Mater. Chem. A*, 2023, **11**, 21099–21108.

25 K. P. Lindquist, S. A. Mack, A. H. Slavney, L. Leppert, A. Gold-Parker, J. F. Stebbins, A. Salleo, M. F. Toney, J. B. Neaton and H. I. Karunadasa, *Chem. Sci.*, 2019, **10**, 10620–10628.

26 F. Ji, Y. Huang, F. Wang, L. Kobera, F. Xie, J. Klarbring, S. Abbrent, J. Brus, C. Yin, S. I. Simak, I. A. Abrikosov, I. A. Buyanova, W. M. Chen and F. Gao, *Adv. Funct. Mater.*, 2020, **30**, 2005521.

27 G. Liu, Z. Zhang, C. Wu, Y. Zhang, X. Li, W. Yu, G. Yao, S. Liu, J. Shi, K. Liu, Z. Chen, L. Xiao and B. Qu, *Adv. Funct. Mater.*, 2022, **32**, 2109891.

28 Z. Li, S. R. Kavanagh, M. Napari, R. G. Palgrave, M. Abdi-Jalebi, Z. Andaji-Garmaroudi, D. W. Davies, M. Laitinen, J. Julin, M. A. Isaacs, R. H. Friend, D. O. Scanlon, A. Walsh and R. L. Z. Hoye, *J. Mater. Chem. A*, 2020, **8**, 21780–21788.

29 F. Ji, F. Wang, L. Kobera, S. Abbrent, J. Brus, W. Ning and F. Gao, *Chem. Sci.*, 2021, **12**, 1730–1735.

30 H. Yin, Y. Xian, Y. Zhang, W. Chen, X. Wen, N. U. Rahman, Y. Long, B. Jia, J. Fan and W. Li, *Adv. Funct. Mater.*, 2020, **30**, 2002225.

31 Z. Liu, Y. Sun, T. Cai, H. Yang, J. Zhao, T. Yin, C. Hao, M. Chen, W. Shi, X. Li, L. Guan, X. Li, X. Wang, A. Tang and O. Chen, *Adv. Mater.*, 2023, **35**, 2211235.

32 F. Locardi, M. Cirignano, D. Baranov, Z. Dang, M. Prato, F. Drago, M. Ferretti, V. Pinchetti, M. Fanciulli, S. Brovelli, L. De Trizio and L. Manna, *J. Am. Chem. Soc.*, 2018, **140**, 12989–12995.

33 Y. Liu, Y. Jing, J. Zhao, Q. Liu and Z. Xia, *Chem. Mater.*, 2019, **31**, 3333–3339.

34 F. Locardi, E. Sartori, J. Buha, J. Zito, M. Prato, V. Pinchetti, M. L. Zaffalon, M. Ferretti, S. Brovelli, I. Infante, L. De Trizio and L. Manna, *ACS Energy Lett.*, 2019, **4**, 1976–1982.

35 R. Ahmad, L. Zdražil, S. Kalytchuk, A. Naldoni, E. Mohammadi, P. Schmuki, R. Zboril and Š. Kment, *Appl. Mater. Today*, 2022, **26**, 101288.

36 R. Ahmad, L. Zdražil, S. Kalytchuk, A. Naldoni, A. L. Rogach, P. Schmuki, R. Zboril and Š. Kment, *ACS Appl. Mater. Interfaces*, 2021, **13**, 47845–47859.

37 H. Arfin, J. Kaur, T. Sheikh, S. Chakraborty and A. Nag, *Angew. Chem., Int. Ed.*, 2020, **59**, 11307–11311.

38 Y. Zhang, Z. Zhang, W. Yu, Y. He, Z. Chen, L. Xiao, J. Shi, X. Guo, S. Wang and B. Qu, *Advanced Science*, 2022, **9**, 2102895.

39 W. Ning, J. Bao, Y. Puttisong, F. Moro, L. Kobera, S. Shimono, L. Wang, F. Ji, M. Cuartero, S. Kawaguchi, S. Abbrent, H. Ishibashi, R. De Marco, I. A. Bouianova, G. A. Crespo, Y. Kubota, J. Brus, D. Y. Chung, L. Sun, W. M. Chen, M. G. Kanatzidis and F. Gao, *Sci. Adv.*, 2020, **6**, eabb5381.

40 P. Han, C. Luo, W. Zhou, J. Hou, C. Li, D. Zheng and K. Han, *J. Phys. Chem. C*, 2021, **125**, 11743–11749.

41 S. E. Creutz, E. N. Crites, M. C. De Siena and D. R. Gamelin, *Nano Lett.*, 2018, **18**, 1118–1123.

42 J. Heyd, G. E. Scuseria and M. Ernzerhof, *J. Chem. Phys.*, 2003, **118**, 8207–8215.

43 J. Heyd and G. E. Scuseria, *J. Chem. Phys.*, 2004, **121**, 1187–1192.

44 E. E. Salpeter and H. A. Bethe, *Phys. Rev.*, 1951, **84**, 1232–1242.

45 S. Albrecht, L. Reining, R. Del Sole and G. Onida, *Phys. Rev. Lett.*, 1998, **80**, 4510–4513.

46 M. Rohlfing and S. G. Louie, *Phys. Rev. Lett.*, 1998, **81**, 2312–2315.

47 S. Shyamal, S. K. Dutta and N. Pradhan, *J. Phys. Chem. Lett.*, 2019, **10**, 7965–7969.

48 Y. Jiang, H. Chen, J. Li, J. Liao, H. Zhang, X. Wang and D. Kuang, *Adv. Funct. Mater.*, 2020, **30**, 2004293.

49 F. Luo, M. Liu, M. Zheng, Q. Li, H. Wang, J. Zhou, Y. Jiang, Y. Yu and B. Jiang, *J. Mater. Chem. A*, 2023, **11**, 241–250.

50 Y.-F. Xu, M.-Z. Yang, B.-X. Chen, X.-D. Wang, H.-Y. Chen, D.-B. Kuang and C.-Y. Su, *J. Am. Chem. Soc.*, 2017, **139**, 5660–5663.

51 J.-N. Huang, Y.-J. Dong, H.-B. Zhao, H.-Y. Chen, D.-B. Kuang and C.-Y. Su, *J. Mater. Chem. A*, 2022, **10**, 25212–25219.

52 Z. Liu, H. Yang, J. Wang, Y. Yuan, K. Hills-Kimball, T. Cai, P. Wang, A. Tang and O. Chen, *Nano Lett.*, 2021, **21**, 1620–1627.

53 G. Yin, X. Qi, Y. Chen, Q. Peng, X. Jiang, Q. Wang, W. Zhang and X. Gong, *J. Mater. Chem. A*, 2022, **10**, 22468–22476.

54 S. S. Bhosale, A. K. Kharade, E. Jokar, A. Fathi, S. Chang and E. W.-G. Diau, *J. Am. Chem. Soc.*, 2019, **141**, 20434–20442.

55 X. Li, Y. Sun, J. Xu, Y. Shao, J. Wu, X. Xu, Y. Pan, H. Ju, J. Zhu and Y. Xie, *Nat. Energy*, 2019, **4**, 690–699.

56 Y. Chai, Y. Kong, M. Lin, W. Lin, J. Shen, J. Long, R. Yuan, W. Dai, X. Wang and Z. Zhang, *Nat. Commun.*, 2023, **14**, 6168.

57 Z. Zhang, D. Li, Z. Dong, Y. Jiang, X. Li, Y. Chu and J. Xu, *Sol. RRL*, 2023, **7**, 2300038.

58 J. Qian, H. Hu, Y. Liang and Z. Zhang, *Appl. Surf. Sci.*, 2024, **648**, 159084.

59 Q. Sun, J. Xu, F. Tao, W. Ye, C. Zhou, J. He and J. Lu, *Angew. Chem., Int. Ed.*, 2022, **61**, e202200872.